Supplementary information to "*Serpentinized peridotite versus thick mafic crust at the Romanche oceanic transform fault*" by Emma Gregory et al.

This document contains the details of methods used in this study (p. 1-7), supplementary table 1 (p. 6), a list of the references cited in this document (p. 7-10) and supplementary figures S1-S9 along with their captions (p. 11-19).

METHODS

OBS data

Along the 400 km-long Romanche section of the seismic profile, 28 OBS recorded a total of 1334 shots fired by an airgun array, with a spacing of 300 m. The airgun array consisted of 16 GGun airguns in two strings, with a total volume of 4990 in^3 (82 L), towed at a depth of 10 m and fired at a pressure of 140 bars. Each OBS was equipped with a hydrophone and 3-component geophone, and were spaced ~14.2 km apart, except for where bathymetric depth did not allow this. The sampling rate was 4 ms and the OBS data are generally of high quality (Supplementary Fig. S1). OBSs were relocated to their seafloor positions using direct water wave picks and a robust least-squares inversion method. Phase identification was aided by processing: predictive deconvolution, bandpass filtering between 4-18 Hz, and a static correction to remove the topographic signature. Travel-times were then manually picked on bandpass-filtered (4-18 Hz) hydrophone data, giving a total of 3127 Pg picks, 4259 Pn picks and 1987 PmP picks. Travel-time errors were assigned based on OBS relocation error, sampling interval and pick uncertainty, and range from 20-82 ms (average 30 ms for Pg; 47 ms for Pn; 51 ms for PmP).

Tomographic modelling

The travel-time dataset was jointly inverted for velocity and a reflection boundary (the Moho) using the method of Van Avendonk et al. (1998, 2004). Here, forward ray-tracing is solved using the shortest-path method, and the inversion problem uses a least-squares approach to update the velocity model. The starting velocity model was created as described as in Marjanović et al. (2020), using multibeam bathymetry and coincident multichannel seismic (MCS) data to constrain the seabed and basement

interfaces, respectively. Sediment velocity is defined as 1.86 km/s, the average from semblance analysis of MCS gathers. The base crustal starting velocity model follows a 1D profile based on White et al. (1992) and Grevemeyer et al. (2018a), with crustal thickness of 6 km. We define the model onto a 200 m x 50 m grid, from the sea surface to 20 km depth.

We followed a top-down, layer-stripping inversion procedure: first inverting the Pg dataset to resolve the upper crustal structure, before introducing PmP picks to resolve the lower crust and Moho depth, and finally inverting the whole dataset together to resolve upper mantle structure. We apply both smoothing and damping constraints during each iteration to keep the model realistic and to avoid artefacts and local fit minima. We reach a final model after a total of nine iterations, finishing with a χ^2 fit of 2.4.

We then follow a Monte Carlo-type procedure to produce 100 possible final models (e.g. Korenaga et al., 2000). An array of 100 starting models is produced by randomly perturbing the crustal thickness (by up to ±1 km), top mantle velocity (up to -0.5/+0.2 km/s), and one crustal velocity parameter (up to ±0.5 km/s) of the base starting velocity model. Subsequently, 100 travel-time datasets are produced by adding random errors to the picked dataset: a common receiver (OBS) error up to 42 ms (the average dataset travel-time error), followed by another error up to 42 ms, differing for each individual pick time. Pairs of the random starting model and travel-time datasets are then inverted using the same procedure and parameters. We take the mean average of the 100 final models to interpret in our study, which has an average χ^2 fit of 2.4.

We use a variety of methods to quantify the coverage, resolution and uncertainty of the final velocity model. The derivative weight sum (Supplementary Fig. S2A - DWS – Toomey & Foulger, 1989) shows good ray coverage of the crustal and upper mantle. Checkerboard tests, performed with anomaly sizes of 25 km x 4 km and 15 km x 3 km at an amplitude of 5%, show good recovery of these anomalies with a little distortion from ray smearing (Supplementary Fig. S2B-E). To quantify the uncertainty in velocity and Moho depth, we take the mean average standard deviation of the 100 final models from the mean model (Supplementary Fig. S2F). Uncertainties in velocity are generally low: varying from 0.1-0.2 km/s in the upper crust to <0.1 km/s in the lower crust, and 0.1-0.2 km/s in the upper mantle. Moho depth

standard deviations vary from ~0.1-0.5 km along the model. To examine whether the model beneath the transform valley, including a velocity contrast at the Moho, is reasonable, we perform 2D finite difference modeling to compute synthetic seismograms. The synthetic data show that a model containing a velocity contrast at the Moho provides a significantly better match to the observed arrivals than a model with smoothly increasing velocity with depth (Supplementary Fig. S4).

Gravity analysis

Gravity data were acquired along the profile during the ILAB-SPARC cruise using a Bondenseewerk KSS31 gravimeter. Marjanović et al. (2020) describe the data corrections and the calculation of the Free-Air Anomaly (FAA – Supplementary Fig. S5A).

In order to perform forward modeling to produce a crustal density model, we then correct the FAA for the gravity anomaly produced by differences in mantle temperature across the transform, due to plate cooling (Kuo & Forsyth, 1988). We use the age of the lithosphere (Müller et al., 2019), bathymetry (GEBCO, 2019), half-spreading rate of 1.75 m/yr, half-space cooling model (Turcotte & Schubert, 2002), and mantle density of 3300 kg/m^3, to calculate the mantle thermal anomaly in the region of the Equatorial Atlantic Ocean. To find the most appropriate value of the mantle thermal expansion coefficient in our study area to use in the calculation, we perform analysis along two flowlines, one from the northern ridge segment and one from the southern. Firstly, we calculate mantle bouguer anomaly (MBA) along the flowlines (Supplementary Fig. S6) and compare the fit of the MBA to the mantle thermal correction calculated using coefficient values ranging from 2.8-4.8 x 10^{-5} K^{-1} (Supplementary Fig. S7a). We find that for the northern flowline, the best-fit value of 4.4 x 10^{-5} K^{-1} is outside the range of possible values for oceanic lithosphere of 3.0-3.8 x 10^{-5} K^{-1} (Afonso et al., 2005), and for the southern profile, although the best-fit value of 3.4 x 10^{-5} K^{-1} is realistic, an insignificant difference in fit (<1 mGal) is found for values ranging from 2.9-3.9 x 10^{-5} K^{-1}. We therefore then estimate the parameter by comparing observed bathymetry with predicted seafloor subsidence, calculated using a half-space cooling model (e.g. Parsons & Sclater, 1977) with different values of the thermal expansion coefficient (Supplementary Fig. S8, S7b). For the half-space cooling model, we use mantle and water densities of 3330 kg/m^3 and 1000 kg/m^3, respectively, a base mantle temperature of

1350°C, thermal conductivity of 3.5 W/m/K, and specific heat capacity of 1170 J/kg/K. Ridge depths are calculated as the average of the west and east ridge wall depths on each flowline and are 2650 m and 2550 m for the northern and southern flowlines, respectively. Using a least-squares fitting algorithm, we find best-fit values of 3.5×10^{-5} K^{-1} for the northern flowline and 3.6×10^{-5} K^{-1} for the southern (Supplementary Fig. S8). As both are realistic values and are similar to one another, we take the average of 3.55×10^{-5} K^{-1} to use in our final calculation of the mantle thermal anomaly. To quantify uncertainty in the thermal anomaly correction caused by potential errors in plate age, we use the age error grid provided by Müller et al. (2008), as there is not one provided with the 2019 version of the model. The greatest errors in age along our profile occur within the transform valley, with an average of ±5.7 Myr, and the resulting errors in the mantle thermal correction are shown in Supplementary Fig. S5A.

Aside from the mantle thermal correction, we also correct the observed FAA for the effect of 3D bathymetry by calculating the difference in the Bouguer correction when using the 2D bathymetry extracted along the model profile and the 2.5D talwani2d GMT program, and the 3D bathymetry from the ship swath grid supplemented by GEBCO satellite data, using GMT's gravfft program. Applying these corrections to the FAA produces the observed, corrected gravity profile, with error bounds resulting from the uncertainty in the mantle thermal correction (Supplementary Fig. S5B).

Subsequently, we convert the final velocity model into a density model, maintaining a constant density in the water (1035 kg/m^3), sediments (1900 kg/m^3), crust (2700 kg/m^3) and mantle (3300 kg/m^3). We use the talwani2d code in GMT, employing the Talwani method (Talwani et al., 1959) for calculating gravity over density anomalies in 2.5D, to calculate FAA over the density model. This uses gravity contrasts as opposed to absolute values, so we then apply a bulk shift to the modelled gravity profile so the mean fit to the observed profile is ~0 mGal (Supplementary Fig. S5B). The constant density model fits the observed profile relatively well (RMS of ~14 mGal), but a clear low gravity anomaly of ~20 mGal is present within the transform valley (considering uncertainties this could potentially vary from -32 to -6 mGal), along with a high gravity anomaly of ~20 mGal south of Romanche (11 to 37 mGal).

We begin forward modelling by adding in a lower density (2500 kg/m^3) upper crust, following the 6.6 km/s (White et al., 1992) contour extracted from the velocity model, which improves the fit along the whole 0-400 km profile, and subsequently re-adjust the bulk shift. This addition effectively introduces a large low-density anomaly into the transform valley. The fit within the valley is further improved through introducing a low-density anomaly (3100 kg/m^3) to the upper mantle, with the extent of the anomalies guided by the velocity anomaly in the final inversion model. The fit to the south of Romanche can be improved through the addition of a high-density anomaly (2700 kg/m^3) to the upper crust, although due to the ambiguity of gravity data this could be equally fit with a lower crust density anomaly. The final RMS fit between the observed and modelled data is 8.2 mGal. As mentioned above, this method is sensitive to the density contrasts as opposed to absolute density, so within the transform valley crust and mantle the interpretable density anomalies are both -200 kg/m^3 from the background crust and mantle densities and in the crust to the south of Romanche the anomaly is +200 kg/m^3 from the background crust density.

Effective medium analysis

In investigate the cause of the Vp anomaly, we undertake an effective medium analysis, following the differential effective medium (DEM) theory (Taylor & Singh, 2002). To simulate fracturing within a transform fault, we add elongate, aligned, fluid-filled fractures, with aspect ratios of 5-100, to a host medium and assess the effect on the physical properties with increasing porosity.

We take the intrinsic properties of the different host media from the literature, with values used summarised in Supplementary Table 1. For mafic material, we use values from laboratory measurements of gabbro samples from the MAR and Oman ophiolite (Hyndman & Drury, 1976; Saito et al., 2015), as we can obtain more reliable, intrinsic 'zero-porosity' parameters for gabbro due to its lack of natural porosity compared to recovered basalts and dolerites. Due to its ubiquity in dredge samples from the eastern Romanche (Seyler & Bonatti, 1997; Tartarotti et al., 2002), we assume melt-impregnated peridotite (MIP) is the dominant peridotite composition within the transform valley, and include unaltered peridotite for the composition beneath the surrounding crust. For these lithologies, we use modal and mineral compositions from dredged sample analyses from Romanche TF to predict

the physical properties using the toolbox from Abers & Hacker (2016). We average the composition of samples from Tartarotti et al. (2002) for a melt-impregnated peridotite composition of 59.2% olivine (90% Fo, 10% Fa), 16.5% orthopyroxene (90% En, 10% Fs), 11.8% clinopyroxene (Di), 1.5% spinel and 11% plagioclase (90% An, 10% Ab). We use the composition of the undepleted lherzolite from eastern Romanche from Seyler & Bonatti (1997), similar to the western Romanche undepleted lherzolites, for an unaltered peridotite composition of 65.2% olivine (90% Fo, 10% Fa), 22.3% orthopyroxene (90% En, 10% Fs), 10.8% clinopyroxene (Di) and 1.7% spinel. For the properties of serpentinized melt-impregnated peridotite, we take standard Vp and density changes from serpentinization for 'standard' peridotite (~90% olivine harzburgite) of -3 km/s in Vp and -700 kg/m3 in density for 100% serpentinization (e.g. Roland et al., 2012), and scale these for the olivine composition of the melt-impregnated peridotite. This assumes that the alteration of olivine to serpentine is the dominant reaction with the greatest effect on the physical properties. We then use a Vp/Vs value of 2.0 to calculate the Vs (after Grevemeyer et al., 2018b; Christensen, 1966).

Supplementary Table 1: Intrinsic physical properties used for different lithologies in DEM analyses

	Vp (km/s)	**Vs (km/s)**	**Density (kg/m^3)**
Gabbro	7.00	3.83	3000
Unaltered peridotite	8.23	4.80	3316
Melt-impregnated peridotite (MIP)	8.05	4.65	3252
100% serpentinized MIP	6.13	3.07	2804

We use the intrinsic physical properties of each lithology as the properties of the host medium in the DEM calculations. We add increasing proportions of fractures with aspect ratios of 1, 5, 10 and 100 and plot the porosity against the resultant P-wave velocity and density (Supplementary Fig. S9). To assess the cause of the crustal low velocity anomaly, we compare the DEM results for gabbro and 100% serpentinized MIP with the range of Vp observed in the transform valley crust. We also show the effect of progressive serpentinization on the velocity of MIP. To further quantify the causes of the transform valley anomalies, we show the change in density associated with the increasing porosity for different

lithologies (Supplementary Fig. S9b), compared with the density anomalies within the crust and mantle as modelled using the gravity data.

REFERENCES CITED

Abers, G. A., & Hacker, B. R. (2016). A MATLAB toolbox and Excel workbook for calculating the densities, seismic wave speeds, and major element composition of minerals and rocks at pressure and temperature. *Geochemistry, Geophysics, Geosystems*, *17*(2), 616–624. https://doi.org/10.1002/2015GC006171

Afonso, J. C., Ranalli, G., & Fernàndez, M. (2005). Thermal expansivity and elastic properties of the lithospheric mantle: Results from mineral physics of composites. *Physics of the Earth and Planetary Interiors*, *149*(3–4), 279–306. https://doi.org/10.1016/j.pepi.2004.10.003

Christensen, N. I. (1966). Elasticity of ultrabasic rocks. *Journal of Geophysical Research*, *71*(24), 5921–5931. https://doi.org/10.1029/JZ071i024p05921

Grevemeyer, I., Ranero, C. R., & Ivandic, M. (2018a). Structure of oceanic crust and serpentinization at subduction trenches. *Geosphere*, *14*(2), 1–24. https://doi.org/10.1130/GES01537.1

Grevemeyer, I., Hayman, N. W., Peirce, C., Schwardt, M., Van Avendonk, H. J. A., Dannowski, A., & Papenberg, C. (2018b). Episodic magmatism and serpentinized mantle exhumation at an ultraslow-spreading centre. *Nature Geoscience*, *11*(6), 444–448. https://doi.org/10.1038/s41561-018-0124-6

Hyndman, R. D., & Drury, M. J. (1976). The physical properties of oceanic basement rocks from deep drilling on the Mid-Atlantic Ridge. *Journal of Geophysical Research*, *81*(23), 4042–4052. https://doi.org/10.1029/JB081i023p04042

Korenaga, J., Holbrook, W. S., Kent, G. M., Kelemen, P. B., Detrick, R. S., Larsen, H. C., Hopper, J. R., & Dahl-Jensen, T. (2000). Crustal structure of the southeast Greenland margin from joint

refraction and reflection seismic tomography. *Journal of Geophysical Research: Solid Earth*, *105*(B9), 21591–21614. https://doi.org/10.1029/2000jb900188

Kuo, B.-Y., & Forsyth, D. W. (1988). Gravity Anomalies of the Ridge-Transform System in the South Atlantic Between 31 and 34.5° S: Upwelling Centers and Variations in Crustal Thickness. *Marine Geophysical Researches*, *10*, 205–232.

Marjanović M., Singh, S. C., Gregory, E. P. M., Grevemeyer, I., Growe, K., Vaddineni, V., Laurencin, M., Carton, H., Gómez de la Peña, L., & Filbrandt, C. Seismic Crustal Structure and Morpho-tectonic Features Associated with the Chain Fracture Zone and their Role in the Evolution of the Equatorial Atlantic Region. *Journal of Geophysical Research: Solid Earth.*

Müller, R. D., Sdrolias, M., Gaina, C., & Roest, W. R. (2008). Age, spreading rates, and spreading asymmetry of the world's ocean crust. *Geochemistry, Geophysics, Geosystems*, *9*(4), 1–19. https://doi.org/10.1029/2007GC001743

Müller, R. D., Zahirovic, S., Williams, S. E., Cannon, J., Seton, M., Bower, D. J., Tetley, M. G., Heine, C., Le Breton, E., Liu, S., Russell, S. H. J., Yang, T., Leonard, J., & Gurnis, M. (2019). A Global Plate Model Including Lithospheric Deformation Along Major Rifts and Orogens Since the Triassic. *Tectonics*, *38*(6), 1884–1907. https://doi.org/10.1029/2018TC005462

Parsons, B., & Sclater, J. G. (1977). An analysis of the variation of ocean floor bathymetry and heat flow with age. *Journal of Geophysical Research*, *82*(5), 803–827. https://doi.org/10.1029/jb082i005p00803

Saito, S., Ishikawa, M., Arima, M., & Tatsumi, Y. (2015). Laboratory measurements of 'porosity-free' intrinsic *Vp* and *Vs* in an olivine gabbro of the Oman ophiolite: Implication for interpretation of the seismic structure of lower oceanic crust. *Island Arc*, *24*(2), 131–144. https://doi.org/10.1111/iar.12092

Seyler, M., & Bonatti, E. (1997). Regional-scale melt-rock interaction in lherzolitic mantle in the Romanche Fracture Zone (Atlantic Ocean). *Earth and Planetary Science Letters*, *146*, 273–287.

Talwani, M., Worzel, J. L., & Landisman, M. (1959). Rapid Gravity Computations for Two-Dimensional Bodies with Application to the Mendocino Submarine Fracture Zone. *Journal of Geophysical Research*, *64*(1).

Tartarotti, P., Susini, S., Nimis, P., & Ottolini, L. (2002). Melt migration in the upper mantle along the Romanche Fracture Zone (Equatorial Atlantic). In *Lithos* (Vol. 63). www.elsevier.com/locate/lithos

Taylor, M. A. J., & Singh, S. C. (2002). Composition and microstructure of magma bodies from effective medium theory. *Geophysical Journal International*, *149*(1), 15–21. https://doi.org/10.1046/j.1365-246X.2002.01577.x

Toomey, D. R., & Foulger, G. R. (1989). Tomographic inversion of local earthquake data from the Hengill- Grensdalur central volcano complex, Iceland. *Journal of Geophysical Research*, *94*(B12). https://doi.org/10.1029/jb094ib12p17497

Turcotte, D. L., & Schubert, G. (2002). *Geodynamics*. Cambridge University Press.

Van Avendonk, H. J. A., Harding, A. J., Orcutt, J. A., & McClain, J. S. (1998). A two-dimensional tomographic study of the Clipperton transform fault. *Journal of Geophysical Research: Solid Earth*, *103*(B8), 17885–17899. https://doi.org/10.1029/98JB00904

Van Avendonk, H. J. A., Shillington, D. J., Holbrook, W. S., & Hornbach, M. J. (2004). Inferring crustal structure in the Aleutian island arc from a sparse wide-angle seismic data set. *Geochemistry, Geophysics, Geosystems*, *5*(8). https://doi.org/10.1029/2003GC000664

White, R. S., McKenzie, D., & O'Nions, R. K. (1992). Oceanic crustal thickness from seismic measurements and rare earth element inversions. *Journal of Geophysical Research, 97*(B13), 19683–19715. https://doi.org/10.1029/92JB01749

SUPPLEMENTARY FIGURES AND CAPTIONS

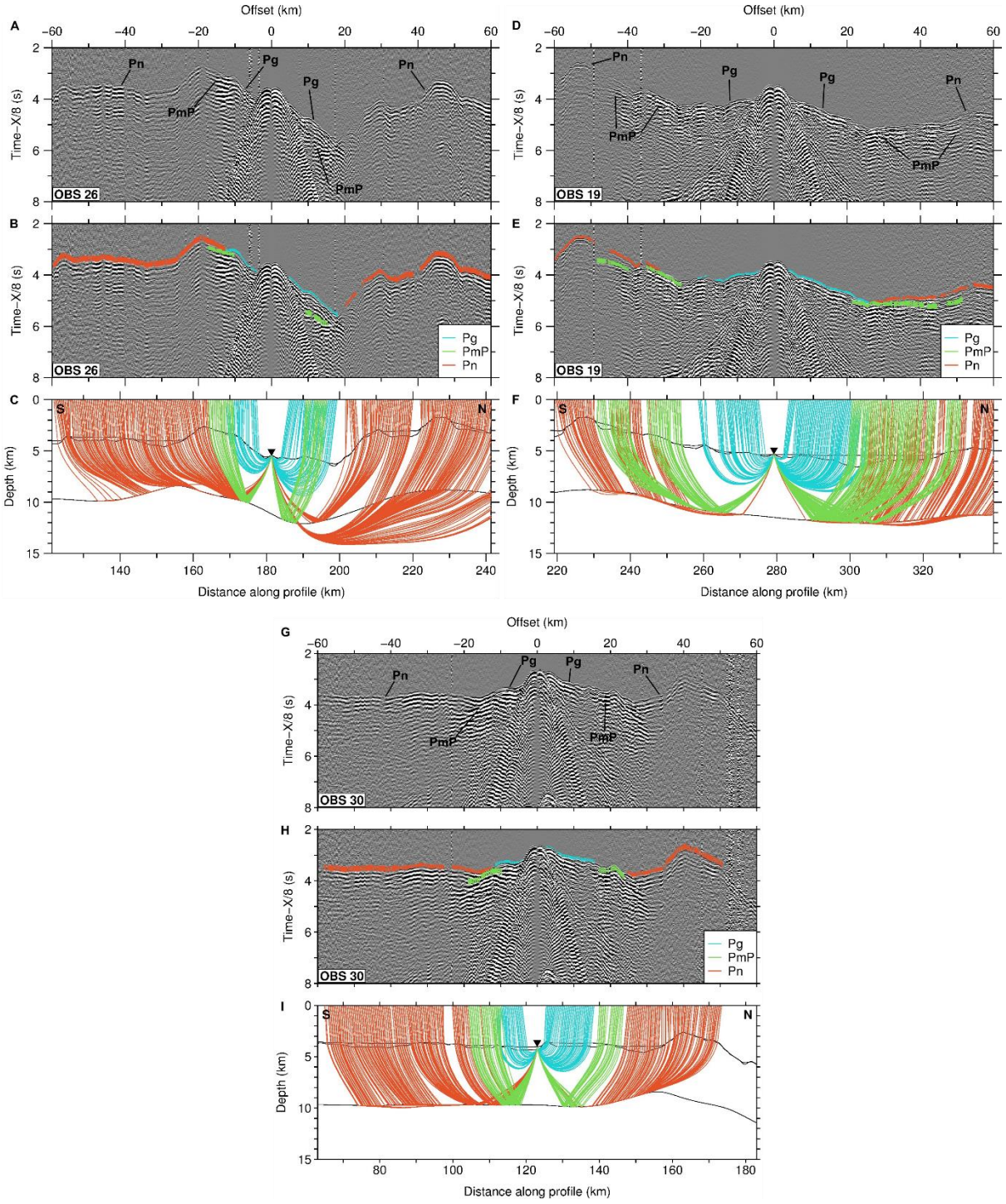

Supplementary figure S1: OBS records and ray tracing. A. Record section for OBS26, located within Romanche transform valley, with identified phases. B. Travel time picks, width of line indicates pick uncertainty. C. Ray tracing through final velocity model, with ray colour matching the picks in B. D, E and F show the same for OBS19, as an example over normal magmatic crust to the north of Romanche, and G, H and I for OBS30, as an example over thinner, tectonic crust to the south of Romanche.

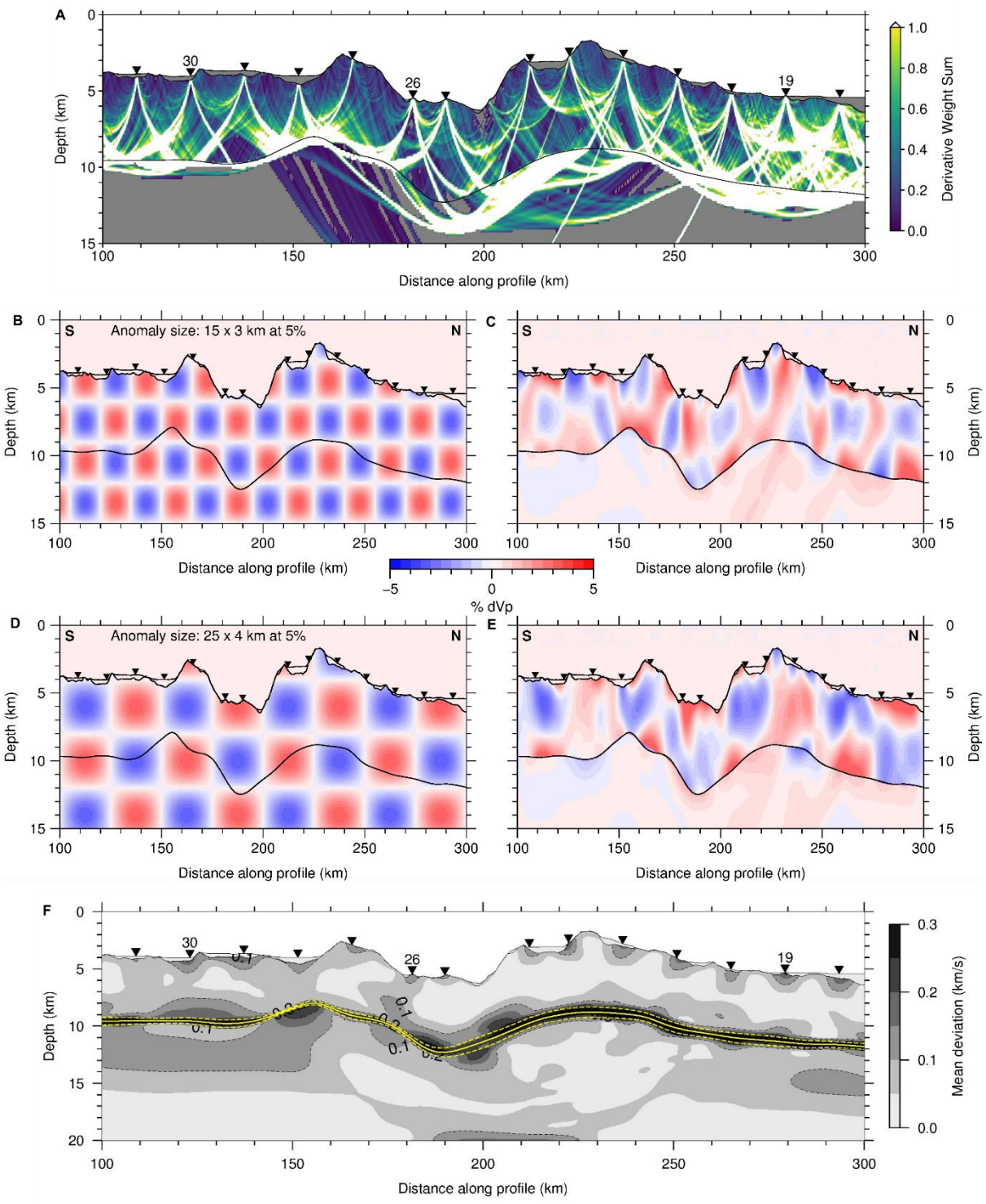

252

253 **Supplementary figure S2:** A. Derivative Weight Sum plot of final tomography model, showing good
254 crustal ray coverage. B-E. Checkerboard test input checkerboards (B, D) and recovered checkerboards
255 (C, E). F. Mean standard deviation from the average final velocity model. The average Moho is shown
256 in yellow solid line, with its mean deviation shown in yellow dashed line.

257

258

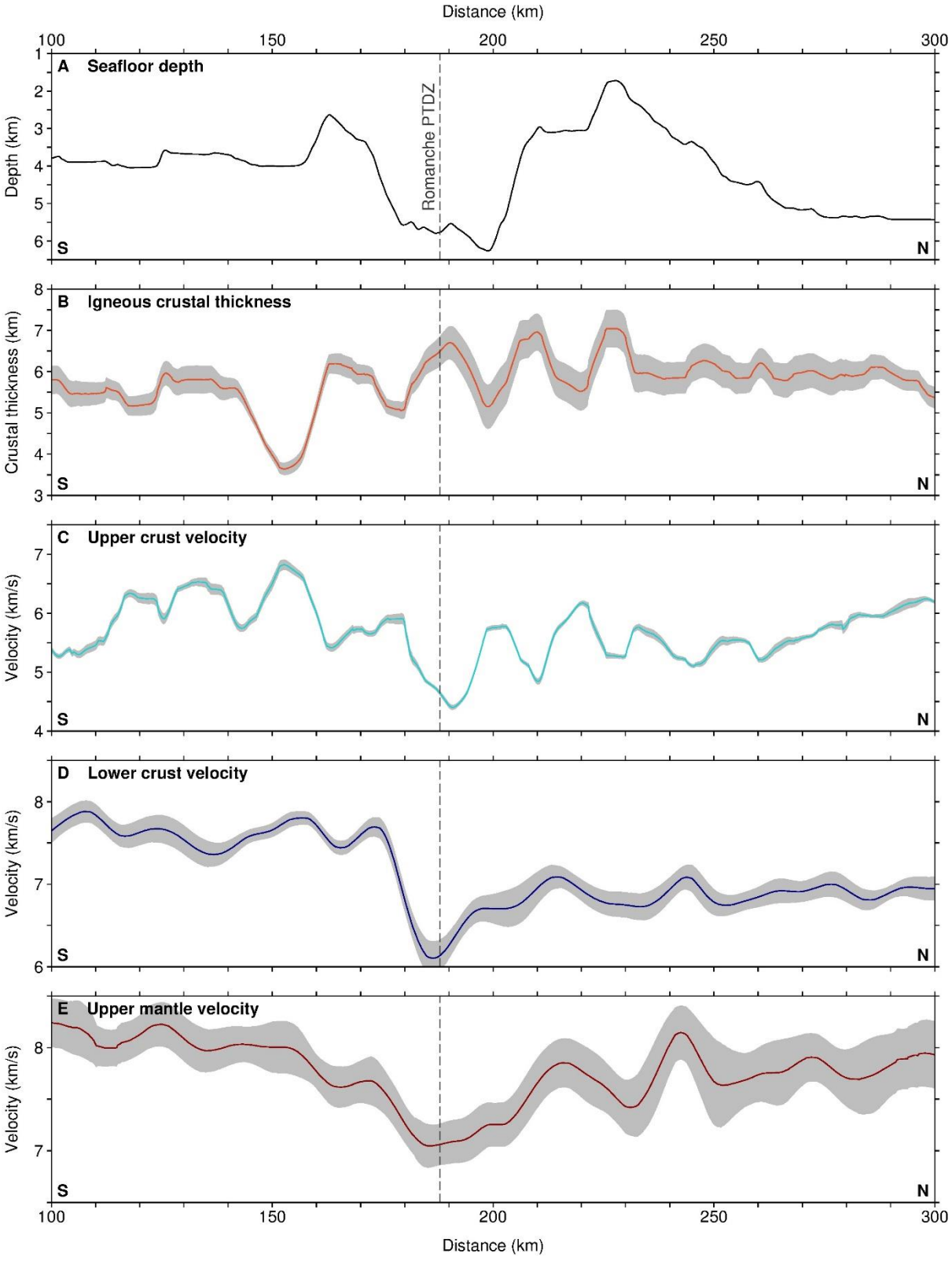

Supplementary figure S3: Key characteristics from the final velocity model. A. Seafloor depth from swath bathymetry. B. Crustal thickness from top basement to Moho. C. Average upper crust velocity (top 3 km of crust). D. Average lower crust velocity (2 km of crust above Moho). E. Average upper mantle velocity (top 0.5 km of mantle). Standard deviation from the average final model is shown by the grey bands.

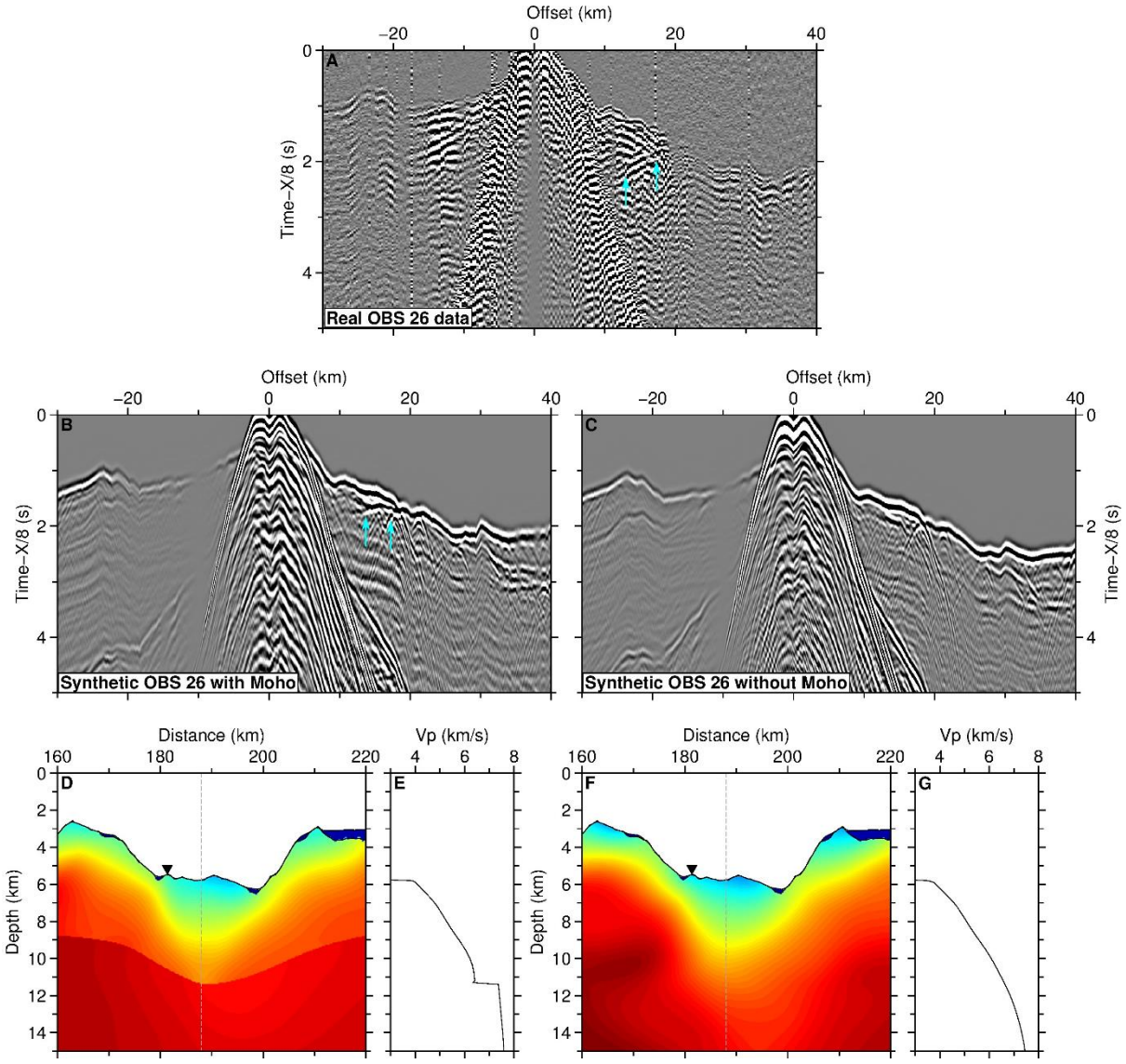

Supplementary figure S4: Synthetic modeling of seismograms, illustrating that a model with a velocity contrast at the Moho produces a seismogram containing PmP arrivals, consistent with the observed data. A. Observed data from OBS 26, PmP reflections marked by blue arrows. B. Synthetic seismogram of OBS 26 produced through finite difference modeling using a model containing a Moho (see D., E.). PmP arrivals marked by blue arrows. C. Synthetic seismogram produced using a model without a Moho, with gradually increasing velocity with depth (see F., G.). D. and F. Tomographic models used to produce the seismograms in B. and C., respectively. The grey dashed lines show the location of the 1D velocity-depth profiles shown in E. and G. Black triangle is the position of OBS 26. Static shifts have been applied to the OBS data shown here to remove the effect of seafloor topography.

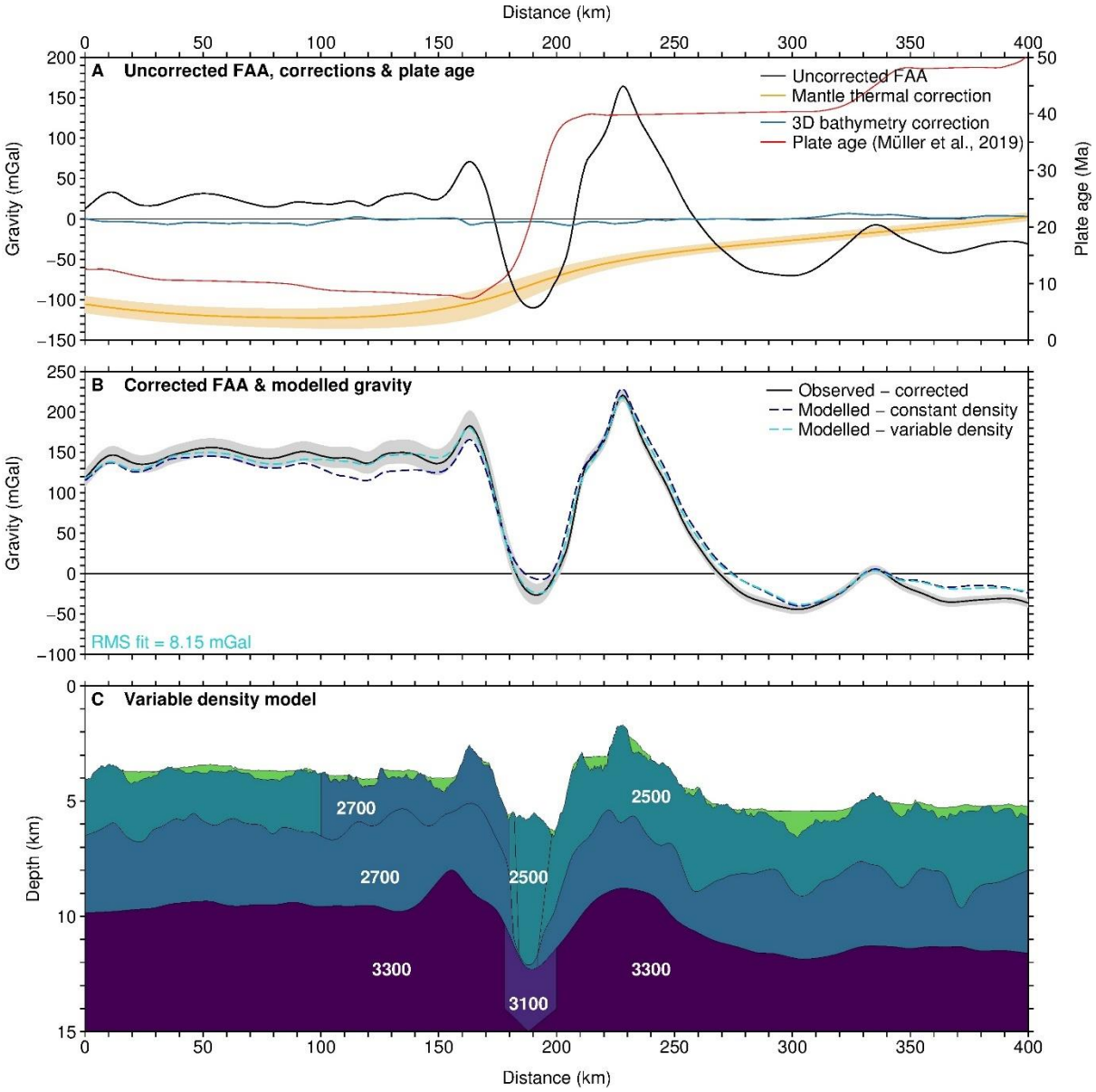

Supplementary figure S5: Gravity modelling. A. Observed, uncorrected Free-Air Anomaly (FAA - black) from shipboard gravimeter, alongside the corrections to compensate for the mantle thermal gravity anomaly (orange – uncertainty bounds shown in pale orange), and the effect of bathymetric features not on the 2D profile (blue). Also shown is the plate age used for the mantle thermal anomaly calculation (red), extracted along the profile. B. Observed, corrected FAA gravity from shipboard gravimeter (black – uncertainty bounds shown in grey), corrected for the thermal effect of lithospheric cooling from the age contrast across the transform fault and the effects of 3D bathymetry. Calculated gravity (dark blue dashed) using a constant density crust, with thickness defined by the velocity model. Calculated gravity (light blue dashed) using a variable density model containing anomalies (see C). C. The variable density anomaly produced to match the observed gravity, with the upper/lower crust boundary defined using the 6.6 km/s contour from the velocity model. There are three density anomalies: 1. The whole crust inside the valley is at upper crust density (2500 kg/m3), which is -200 kg/m3 from lower crust density; 2. Mantle anomaly below the valley is -200 kg/m3 from the rest of the mantle; 3. Upper crust to the south of Romanche is +200 kg/m3 as compared to the normal upper crust.

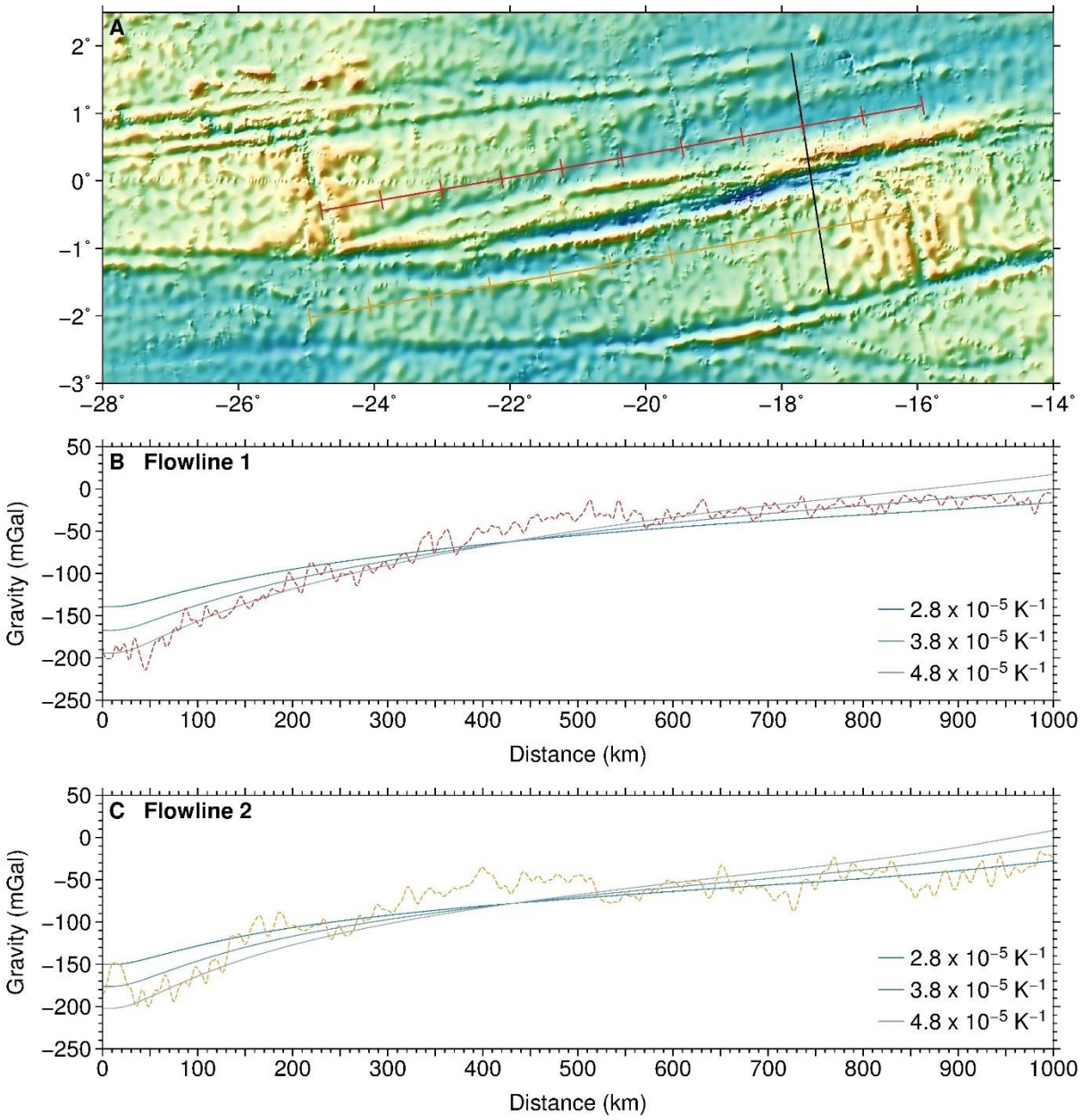

Supplementary figure S6: Analysis of the mantle thermal expansion coefficient parameter using mantle bouguer anomalies. A. Bathymetric map of the study area showing the location of the two flowlines used (red and orange lines, every 100 km marked with a tick), in relation to the seismic profile (black line). B. Mantle bouguer anomaly calculated along flowline 1 (red dashed line; red line in A), using a 6 km-thick crust and densities of 1035 kg/m^3, 2700 kg/m^3 and 3300 kg/m^3 for water, crust and mantle, respectively. The mantle thermal gravity anomalies calculated using different thermal expansion coefficients are shown in blue. C. Same as in B for flowline 2 (orange dashed line; orange line in A).

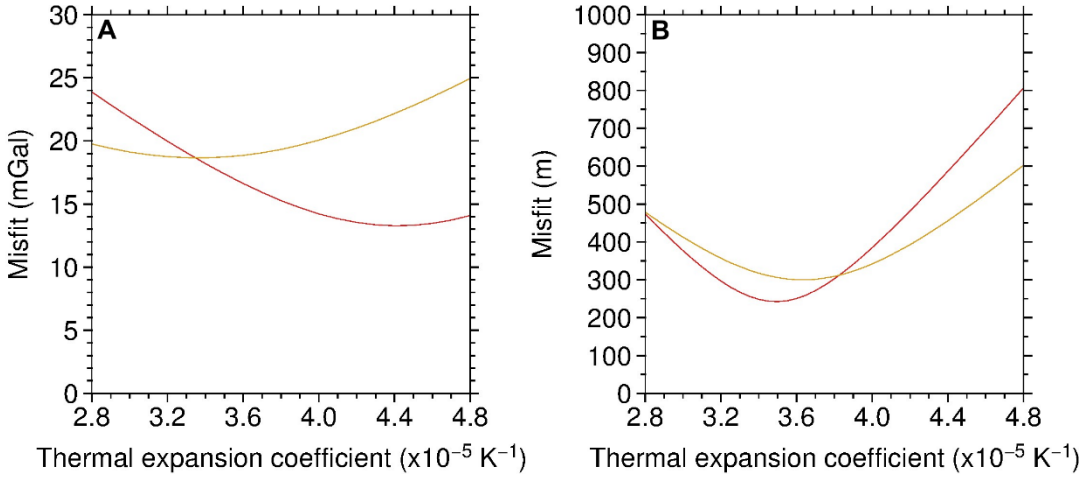

Supplementary figure S7: Misfit analysis of using different thermal expansion coefficients. A. Misfit between mantle bouguer anomaly and calculated mantle thermal gravity correction using different values for the coefficient for flowline 1 (red line) and flowline 2 (orange line). B. Misfit between observed bathymetry and calculated seafloor depth using a half-space cooling model and different values for the coefficient for flowline 1 (red line) and flowline 2 (orange line).

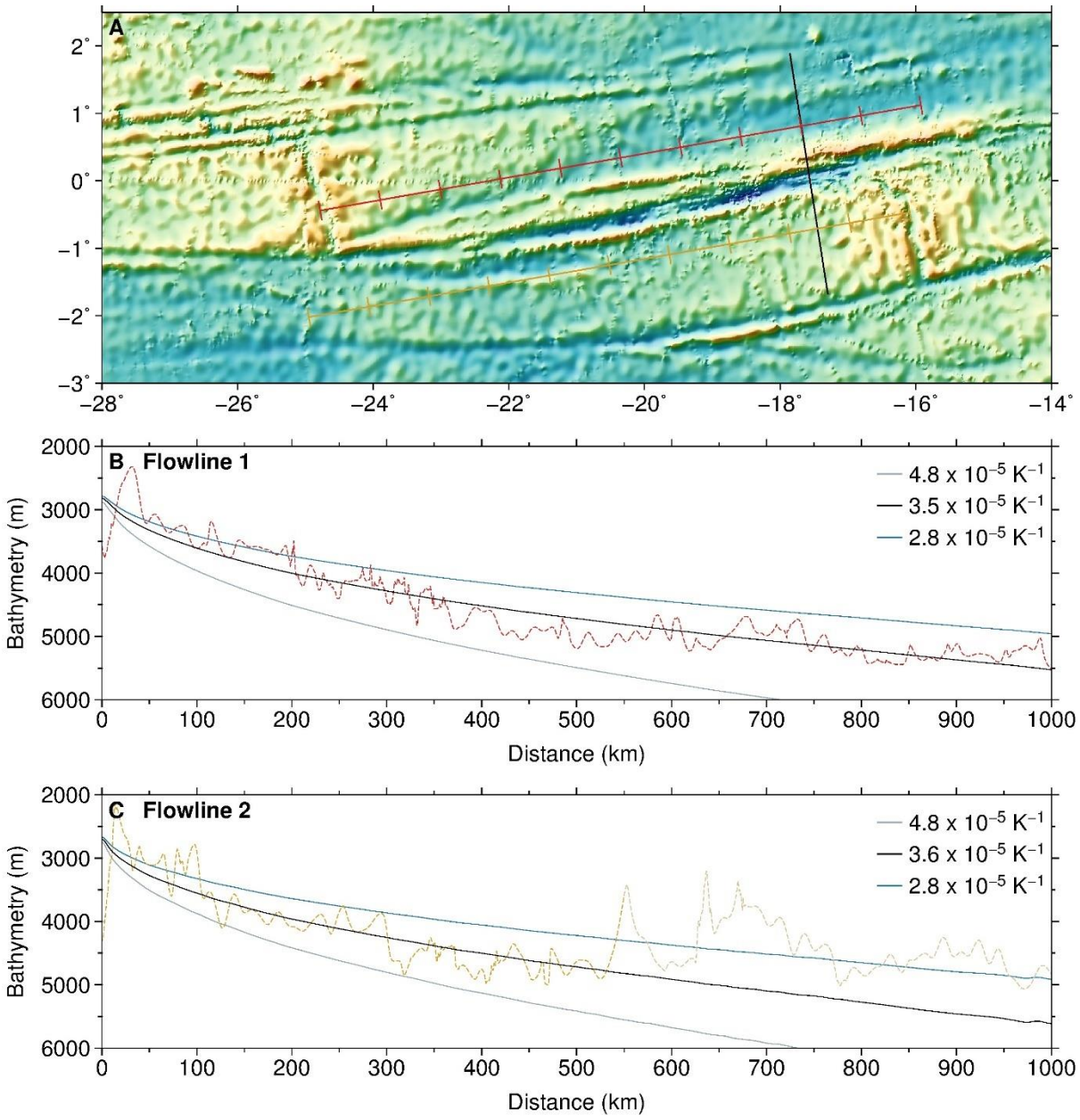

Supplementary figure S8: Analysis of the thermal expansion coefficient parameter using seafloor subsidence. A. Bathymetric map of the study area showing the location of the two flowlines used (red and orange lines, every 100 km marked with a tick), in relation to the seismic profile (black line). B. Bathymetric profile along flowline 1 (red dashed line; red line in A). Predictions of seafloor subsidence using a half-space cooling model and different thermal expansion coefficients are shown in blue (maximum and minimum values) and black (best-fit value). C. Same as in B for flowline 2 (orange dashed line; orange line in A). Here we only used the first 550 km (29 Myr) of the profile (shown in darker orange) as beyond this the flowline is disturbed by a propagator.

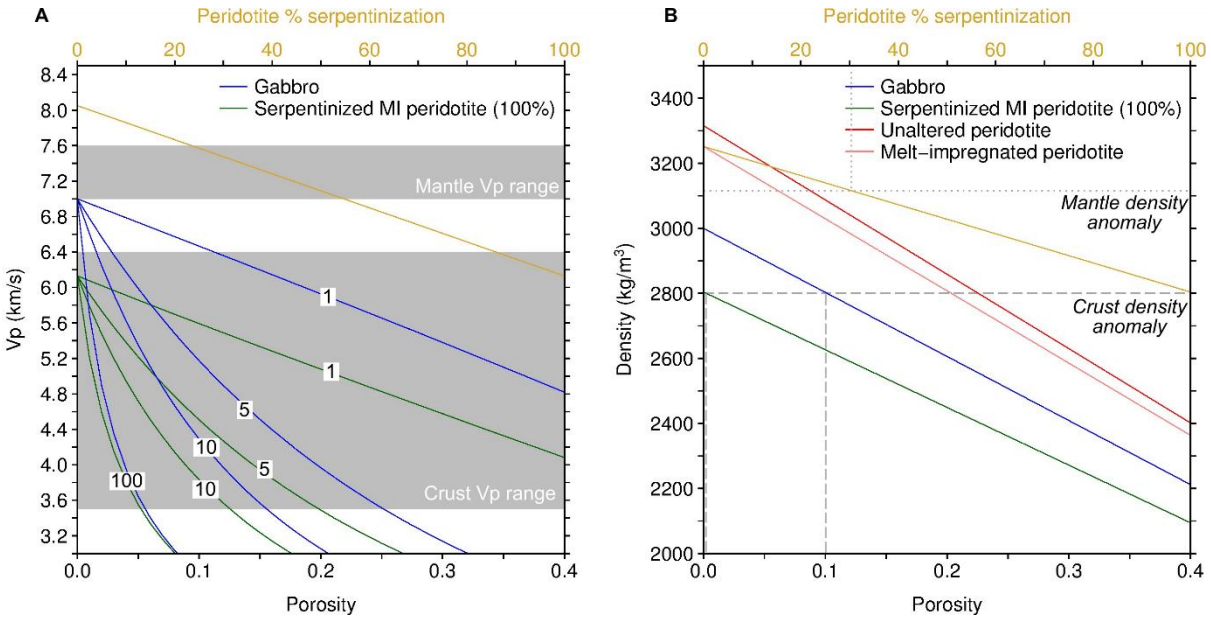

Supplementary figure S9: Effective medium and density analyses. A. Porosity-velocity results from differential effective medium analysis (Taylor & Singh, 2002), assuming aligned fluid-filled fractures in either a gabbro or 100% serpentinized melt-impregnated (MI) peridotite matrix, at a range of crack aspect ratios (indicated by numbered labels). Grey shading shows the Vp range of the transform valley crust and mantle in the velocity model. Fracturing within either gabbro or MI peridotite is necessary to explain the crustal Vp range, with slightly less maximum porosity required for MI peridotite (12% vs 15% for aspect ratio of 10). A minimum porosity of 5% is required to explain the lowest velocities considering an aspect ratio of 100. Also shown in yellow is % serpentinization vs Vp for altered MI peridotite. Approximately 25-55% serpentinization is required to explain the mantle Vp range. B. Porosity-density relationships for gabbro, 100% and 0% serpentinized MI peridotite, and the unaltered, fertile lherzolite peridotite, alongside the % serpentinization-density relationship for MI peridotite. Shown in grey dashed are the transform valley crust and mantle density anomalies from gravity modelling. The anomalies (both -200 kg/m^3), are shown relative to the background composition of undepleted lherzolite for the mantle and gabbro for the crust. The crustal density anomaly is consistent with ~10% porosity gabbro or 0% porosity serpentinized MI peridotite. The mantle density anomaly is consistent with ~30% serpentinized MI peridotite.